

PAPER

Metallographic autopsies of full-scale ITER prototype cable-in-conduit conductors after full testing in SULTAN: 1. The mechanical role of copper strands in a CICC

To cite this article: Carlos Sanabria *et al* 2015 *Supercond. Sci. Technol.* **28** 085005

View the [article online](#) for updates and enhancements.

You may also like

- [Contact mechanical characteristics of Nb₃Sn strands under transverse electromagnetic loads in the CICC cross-section](#)
Ji Yue Zhu, Wei Luo, You He Zhou et al.
- [Performance test and analysis of the first large-scale cable-in-conduit conductor with high J_c Nb₃Sn strand for fusion reactor](#)
Chao Dai, Yu Wu, Jiangang Li et al.
- [Examination of design parameters affecting Nb₃Sn CICC current sharing temperature using necessary condition analysis](#)
Soun Pil Kwon

Metallographic autopsies of full-scale ITER prototype cable-in-conduit conductors after full testing in SULTAN: 1. The mechanical role of copper strands in a CICC

Carlos Sanabria¹, Peter J Lee¹, William Starch¹, Timothy Blum¹,
Arnaud Devred², Matthew C Jewell^{2,3}, Ian Pong^{2,4},
Nicolai Martovetsky⁵ and David C Larbalestier¹

¹ Applied Superconductivity Center, NHMFL, Florida State University, Tallahassee, FL 32310, USA

² ITER International Fusion Energy Organization, Route de Vinon sur Verdon, F-13115 Saint Paul lez Durance, France

³ The Materials Science Center, University of Wisconsin Eau Claire, Eau Claire, WI 54702, USA

⁴ Now at the Accelerator Technology & Applied Physics Division, Lawrence Berkeley National Laboratory, 1 Cyclotron Road, Berkeley, CA 94720-8201, USA

⁵ ORNL, US ITER, Oak Ridge, TN 37831, USA

E-mail: sanabria@asc.magnet.fsu.edu

Received 24 April 2015, revised 26 May 2015

Accepted for publication 29 May 2015

Published 22 June 2015



CrossMark

Abstract

Cables made with Nb₃Sn-based superconductor strands will provide the 13 T maximum peak magnetic field of the ITER central solenoid (CS) coils and they must survive up to 60 000 electromagnetic cycles. Accordingly, prototype designs of CS cable-in-conduit-conductors (CICC) were electromagnetically tested over multiple magnetic field cycles and warm-up-cool-down scenarios in the SULTAN facility at CRPP. We report here a post-mortem metallographic analysis of two CS CICC prototypes which exhibited some rate of irreversible performance degradation during cycling. The standard ITER CS CICC cable design uses a combination of superconducting and Cu strands, and because the Lorentz force on the strand is proportional to the transport current in the strand, removing the copper strands (while increasing the Cu:SC ratio of the superconducting strands) was proposed as one way of reducing the strand load. In this study we compare the two alternative CICC, with and without Cu strands, keeping in mind that the degradation after the SULTAN test was lower for the CICC without Cu strands. The post-mortem metallographic evaluation revealed that the overall strand transverse movement was 20% lower in the CICC without Cu strands and that the tensile filament fractures found were less, both indications of an overall reduction in high tensile strain regions. It was interesting to see that the Cu strands in the mixed cable design (with higher degradation) helped reduce the contact stresses on the high pressure side of the CICC, but in either case, the strain reduction mechanisms were not enough to suppress cyclic degradation. Advantages and disadvantages of each conductor design are discussed here aimed to understand the sources of the degradation.

Keywords: niobium–tin, ITER, cable-in-conduit conductor, metallography, microscopy

(Some figures may appear in colour only in the online journal)

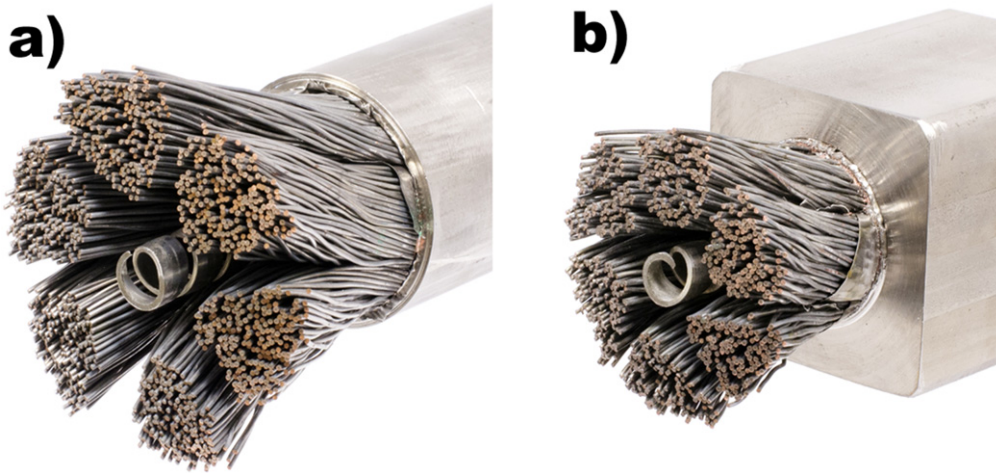


Figure 1. Photographs of (a) the TF conductor and (b) the CS conductor after partial removal of the conductor jackets and petal wraps around each of the six sub-cables in the conduit, making clear the ~ 1000 strands in each conductor. (Photographs are to scale.)

1. Introduction

1.1. ITER magnets and the ITER conductor development program

The ITER magnet system will be the largest superconducting magnet system in the world and with a stored magnetic energy of up to 51 GJ (compared to 11 GJ for the LHC) inside a building as large as the Jefferson memorial in Washington DC, it presents many challenges that have been studied extensively [1]. The possibility of nuclear heating and other electromagnetic (EM) disturbances expected during plasma operation puts a high demand on the cooling system of the superconducting magnets and therefore a cable in conduit conductor (CICC) design was chosen to effectively remove heat [2]. The magnet system will be comprised of four coil systems [3]: the toroidal field (TF) coils, the central solenoid (CS) coils, the poloidal field (PF) coils and the correction coils (CC). The PF and CC systems will have magnetic fields low enough to operate with Nb–Ti, which is the most robust and inexpensive superconductor material available [4]. The TF and CS coils on the other hand, must generate magnetic fields of 11.8 and 13 T respectively, and therefore require higher critical field superconductors, of which Nb₃Sn is by far the most economical [5]. Figure 1 shows photographs of the TF and the CS conductors showing the composite Nb₃Sn strands and copper strands coming out of the steel, force-support and He containment jacket. The cables are fully transposed in order to ensure uniform current distribution.

The use of Nb₃Sn presents an important challenge for the CICC design, mainly because this A15 structured intermetallic is much more sensitive to strain than ductile Nb–Ti [6]. Therefore reversible and irreversible strain effects may degrade the performance if the mechanical effects of the Lorentz force are not properly controlled. The first evidence of uncontrolled degradation in an ITER conductor was found during the testing of the model coils in 2000 [7] when the performance degraded due to strain accumulation as the coils were energized on and off. Although this degradation was a

significant concern, it appeared that the conductor performance would stabilize after about 2000 EM cycles [8].

The fact that the TF coils are to be made using strands made by eight different Nb₃Sn suppliers under ITER contract with different strand architectures makes the CICC production even more challenging. Therefore, it was required to validate all conductor designs before coil fabrication [9] by full qualification tests at the SULTAN (SUpraLeiter TestANlage) testing facility in CRPP, Switzerland [10, 11] where short full-size ITER conductors can be tested in a magnetic field generated by three concentric pairs of superconducting split coils that can provide a homogeneous magnetic field of 10.8 T within 2% over a length of ~ 410 mm [12]. With this magnet at full field, the CICC current can then be ramped up, to match the transverse Lorentz force produced in ITER operation, and subsequently ramped down. Such event is called an EM cycle. In addition to EM cycling SULTAN also allows the temperature to be raised to find the current-sharing temperature, T_{cs} , which is used to qualify the conductor performance at a given EM cycle. A TF CICC qualification run consists in a thousand EM cycles with an occasional T_{cs} check, and this is done until T_{cs} stabilization is achieved *or* the critical number of coil energization cycles is exceeded [13] while still providing an acceptable T_{cs} [1]. By 2010 all the TF conductor designs were validated and despite the fact that some of them did not reach stabilization, all the parties met the requirement of a T_{cs} , higher than 5.8 K after 1000 cycles [14], which is the life expectancy of the TF coils [3]. Accordingly, production of the TF conductor could proceed [9]. Interestingly enough, the TF qualification process showed a wide variety of degradation behavior despite the fact that some conductors were technically identical [15]. There were also a few conductors showing very little sensitivity to cycling [16] which will be an issue addressed in the third article of this study.

The CS coils on the other hand must withstand 60 000 cycles during the 30 000 inductively driven plasma pulses expected from the ITER machine [1, 2, 9], and they therefore present a much greater challenge than the TF coils. In 2010

the first CS prototype, denominated CSJA1, was tested in SULTAN and the T_{cs} fell below the required limit quite rapidly [9, 17]. The autopsy performed on this conductor [17] observed a significant permanent displacement of the strands in the direction of the Lorentz force, leading to the conclusion that the CS design was not optimized against the transverse mechanical effects of the Lorentz force under extended cycle testing. The second CS prototype tested used a ‘3rd generation’ bronze process strand with improved J_c at the cost of a slight increase in hysteresis losses [18]. This design made a slight improvement in the conductor behavior, but it did not show signs of T_{cs} stabilization even after 10 000 cycles [9, 17, 19].

These results raised broad general concerns about the lifetime performance of the CS coils and, in response, a comprehensive R&D program was launched by the ITER International Organization with the support of the US ITER Project Office and the Japan Atomic Energy Agency as the ITER Japan Domestic Agency, as well as Oxford Superconducting Technologies in Carteret, New Jersey, who donated a significant amount of superconducting strand for the production of new CS prototype cables [1, 9]. The task called for a collaboration across many laboratories around the world [9] and a variety of techniques including very sophisticated finite element analysis [20], mechanical testing [21, 22], metallographic analysis [23] and magnetic susceptibility measurements [24]. The program aimed to find the influence of the following conductor parameters: the strand architecture (internal tin versus bronze process), the first triplet configuration (the presence of copper strands) and the cabling twist pitch [19].

1.2. Conductor designs

This paper compares two cables, CSIO1-2 and CSIO1-1. The former had both Cu and superconducting strands and served as a baseline for internal tin conductor performance, while the latter used *only* superconducting strands with an increased Cu to non-Cu ratio of 1.5:1 that resulted in an overall superconducting area increase of about 20% [19] in an attempt to offset the degradation as much as possible. In addition, the design with no Cu strands (CSIO1-1) has the advantage of reducing the force per strand from 919 to 613 N m⁻¹ and it was hoped that this significant reduction in strand-level Lorentz force would reduce the strand peak strain under SULTAN testing. The superconductor-only design of CSIO1-1 was also thought to have the benefit that the composite strands would be stiffer than the pure Cu strands [22] and thus should have more rigidity than CSIO1-2.

The conductor design parameters are listed in table 1. All testing conditions, sample preparation and conductor parameters were essentially identical for both CSIO1-1 and baseline CSIO1-2 with the major exception being the design of the first triplet configuration (Cu strands or not) and the Cu to non-Cu ratio of the strands.

The two different strands of these prototype CICC's are shown in figure 2, while the CICC's T_{cs} degradation profiles are shown in figure 3. The higher initial T_{cs} of the CSIO1-1

Table 1. Relevant CSIO1 conductor parameters.

	CSIO1-1	CSIO1-2
Strand diameter (mm)	0.82	0.82
Cu to non-Cu ratio	1.5:1	1:1
Petal wrap thickness (mm)	0.1	0.1
Petal wrap coverage %	70	70
Cable wrap thickness (mm)	0.1	0.1
Cable wrap overlap %	40	40
Cable layout	3 × 3 × 4 × 4 × 6	3 × 3 × 4 × 4 × 6
First triplet	3SC	2 SC to 1 Cu
Stage 1 twist pitch (mm)	45	45
Stage 2 twist pitch (mm)	85	85
Stage 3 twist pitch (mm)	145	145
Stage 4 twist pitch (mm)	250	250
Stage 5 twist pitch (mm)	450	450
Jacket outer dimensions (mm)	49 × 49	49 × 49
Jacket inner diameter (mm)	32.6	32.6
Spiral outer diameter (mm)	9	9
Calculated void fraction	33.4	33.4

CICC is consistent with its higher overall superconducting area (~40% superconductor in CSIO1-1, compared to ~33.3% in CSIO1-2). It is worth noting that approximations of $T_{cs}(1) - T_{cs}(\infty)$ through data fitting [19, 25] show that the T_{cs} degradation is lower for the CSIO1-1 sample indicating a more robust conductor versus cycling. In this study we have made a detailed quantitative metallographic study to try to understand the mechanism for degradation in the two conductors.

1.3. Introduction to metallographic studies of CICC's

The structural complexity of the samples (CICC's) and the narrow window of observation (last EM cycle evidence) presents many challenges and limitations to this study. Fortunately, as it will be shown below, the sections of conductor which underwent magnetic fields lower than 1 T remain mechanically identical to the sample before SULTAN testing, providing us with an additional data point that can be regarded as zero EM cycles, something that we did not have in our previous CICC autopsy [23]. Unfortunately, solely having a before-and-after picture may not explain the degradation behavior in its entirety, and this is something that needs to be kept in mind at the time of the discussion and conclusion of the study.

The metallographic techniques presented here are not conventional, and although briefly introduced in [23], they will be explained here thoroughly in order to fully demonstrate their capabilities. They consist on two main observations. (1) Transverse cross-section analysis which can provide evidence of permanent transverse movement due to Lorentz force and (2) single strand extraction which can provide evidence of the mechanical effects of the Lorentz force on the composite strands (mainly filament fractures).

Let us remind the reader that filament fractures in Nb₃Sn strands are indications of *very high* stresses and therefore a

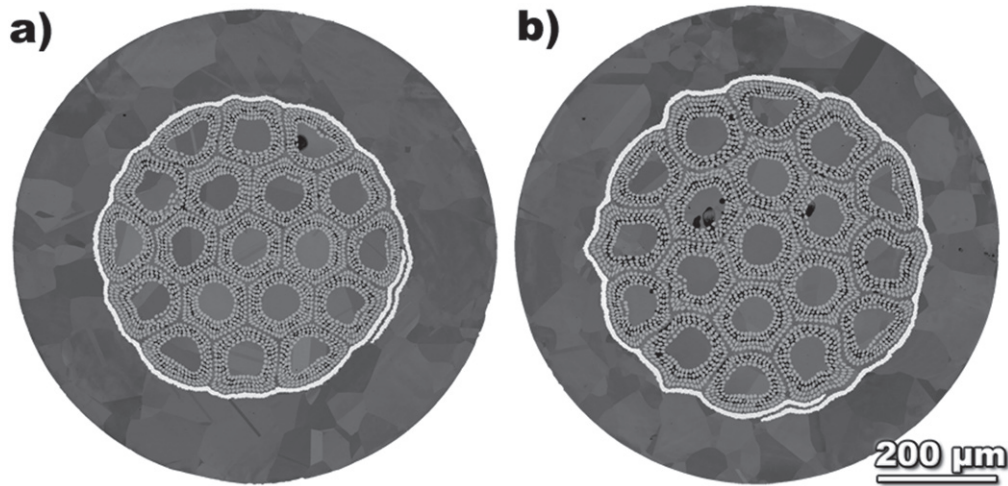


Figure 2. Cross-sections of the OST strands in (a) CSIO1-1 with a Cu-to-non-Cu ratio of 1.5:1 and (b) CSIO1-2 with a Cu-to-non-Cu ratio of 1:1.

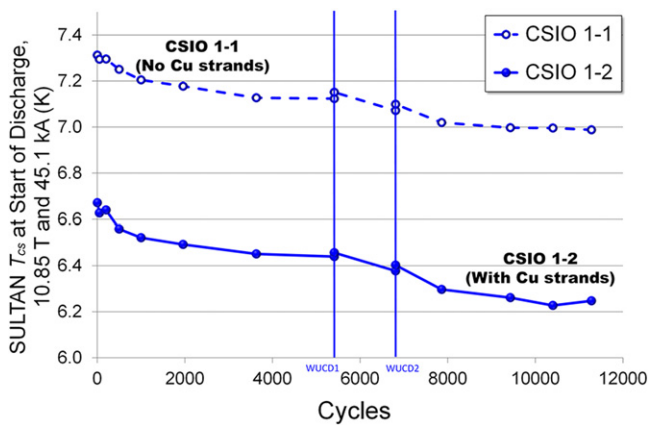


Figure 3. T_{cs} evolution with electromagnetic cycling of the two cable legs analyzed in this paper.

large degradation on the transport current capabilities of the strands, *however*, a great deal of transport current degradation (sometimes as large as 30%) can *still* be induced by bending even when filament fractures are not produced [22], making filament fractures merely the tip of the T_{cs} degradation iceberg. Another consideration is that transport current in extracted strands may not be reliable since the removal of the jacket can alter the strand's stress state significantly [26–28] therefore we focused on metallographic studies only. Despite all these limitations many relevant conclusions can be drawn from these seemingly simple observations.

An additional technique that was not included in [23] will be introduced. It is used to measure the curvature of the extracted strand segments—a curvature which is mostly induced during the cabling and compaction of the CICC.

2. Experimental procedures

After testing in the SULTAN facility in CRPP in Switzerland, the complete legs of both conductors were scribed with their

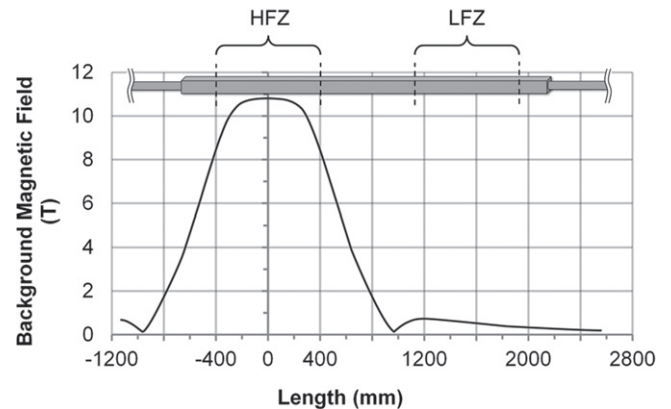


Figure 4. Background magnetic field of the SULTAN magnet [29] along the length of the conductors tested (only one leg is shown).

locations and directions of the Lorentz force, carefully packed and shipped by air to the Applied Superconductivity Center in Florida, USA, for post-mortem examination. In our previous study of a TF conductor [23], we compared cable sections in the center of the high field zone (HFZ) (10.8 T) and an intermediate field zone (~ 9 T) but in the present study we had access to the whole conductor and could compare the HFZ and the low field zones (LFZ < 1 T). Figure 4 shows the magnetic field profile of the SULTAN magnet [29] and the conductor sections studies here designated HFZ and LFZ.

There were two principal aspects of this study:

- A full *transverse cross-section analysis* which used large images to quantify the permanent movement of strands inside the conduit.
- A *strand extraction* study which used longitudinal cross-sections of individual strands extracted from the conductor allowing a detailed description of the strand condition and a search for evidence of Nb₃Sn filament cracking, as well as geometrical distortions of the strands and local cold work in the Cu matrix indicative of local plastic strain in the Cu that must have occurred after heat treatment (i.e. during testing) [30].

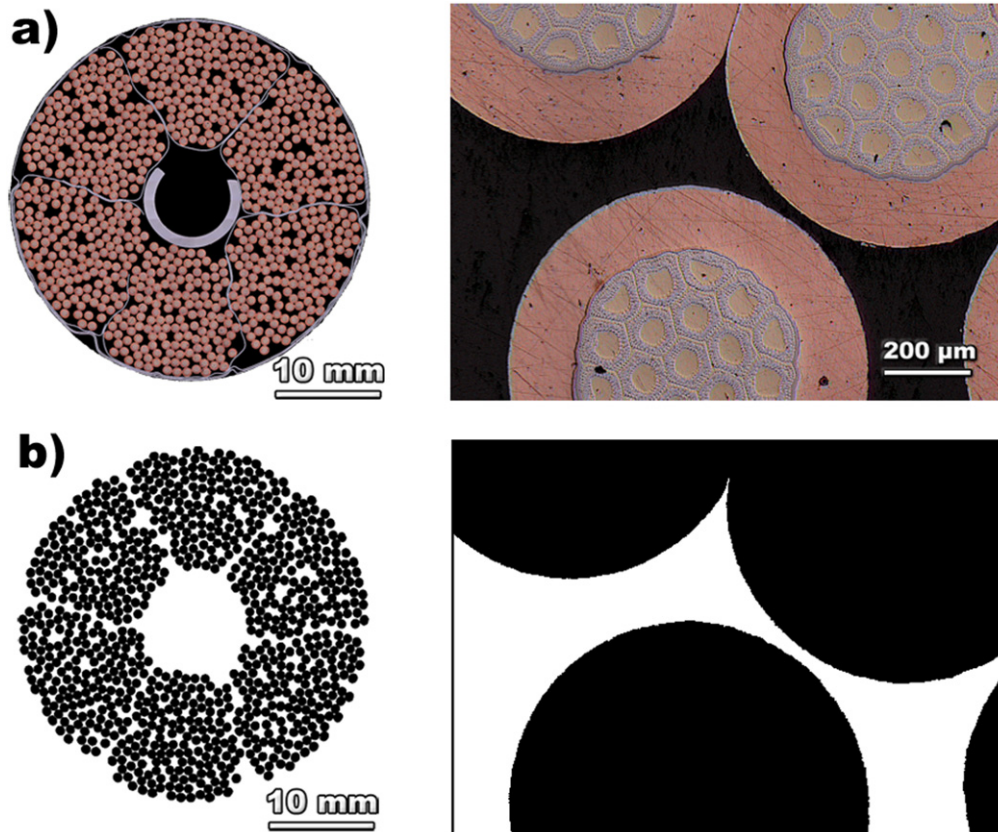


Figure 5. LSCM images of full CICC transverse cross-sections (left) and a closer view (right) showing individual strands. (a) is the original near field scanning laser light microscope image and (b) is the binary image of the strands. Because the stainless steel wrap around each of the six petals has only 70% coverage to allow He flow, there are locations between adjacent petals where there is no clear separation between individual strands of the CICC.

2.1. Transverse cross-section analysis

Two ~ 150 mm long conductor segments (one from the HFZ and one from the LFZ) were cut from each conductor length using electric discharge machining (EDM). These pieces were then vacuum impregnated with epoxy to fill the $\sim 33\%$ void space inside the jacket. Once the epoxy was set, each was further cut using a diamond saw so as to make three cross-sections about 50 mm apart (transposed 40°) of each of the four distinct samples. All were carefully polished and imaged at 50x magnification using a laser scanning confocal microscope (LSCM) with a computer controlled stage that allows taking very large matrices of fully focused images with enough resolution to accurately measure the areas and the coordinate positions of every strand within each CICC. To perform these measurements, the widely used open source software package, Fiji [31] (based on ImageJ [32]) was used to isolate the different components (i.e. strands, void, petal wrap and jacket) into binary (single tone) images like those shown in figure 5(b). Once isolated, a different color was assigned to each component of the image as shown in figure 6(a).

After all components were measured, we calculated the void fraction in each of the six petals or sub-cables, the strand movement and the geometric distortions of the strands. The autopsies performed in [17] and [23] showed that the strands

migrate in the direction of the Lorentz force and therefore a rearrangement of the void fraction is produced. So, in order to quantify the local change in void spacing produced by the Lorentz force we assign an angular value to each petal where 0° (or 360°) marks the circumferential position at which the forces accumulate the most (as the strands migrate in the direction of the Lorentz force), which makes 180° the side of the conductor from which the strands have migrated, as is shown in figure 6(b). We refer to the 0° and 180° positions as the high pressure (HP) and low pressure (LP) conductor sides. Which are (in self-field) slightly lower field and slightly higher field respectively [33].

The void fraction of each petal was measured individually and their deviation from the overall void fraction was used to determine whether the petal had undergone a void fraction expansion (strands moving away from this region) or a void fraction compression (strands moving towards this region). Regions outside the petal wrap (the black features in figure 6(a)) were not assigned to any particular petal and therefore do not play a role in the void deviation measurements but they were taken into account for calculation of the overall void fraction.

Another way to track strand movement within the CICC is by measuring the coordinates of each individual strand with respect to the center of the whole CICC. These geometric

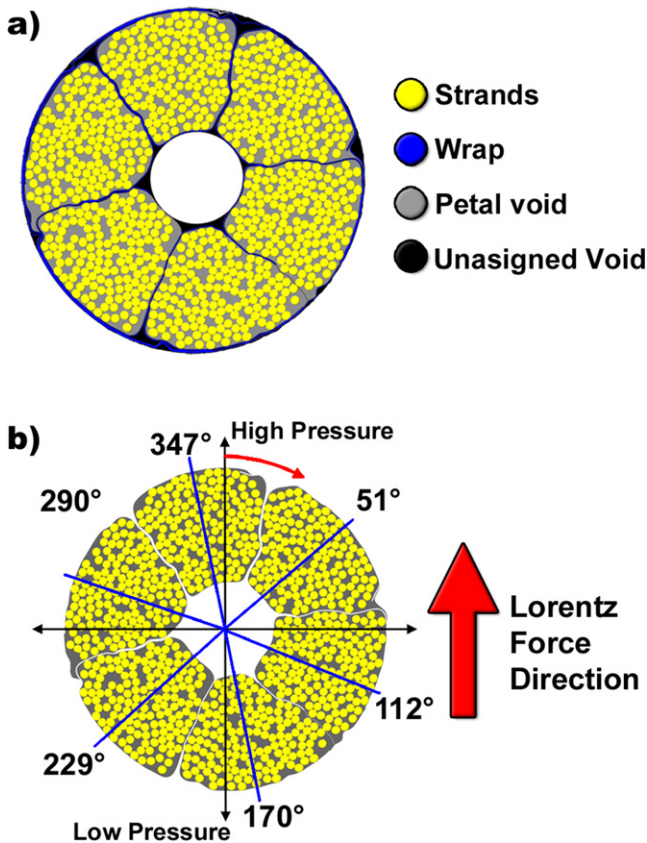


Figure 6. Examples of digitized images of (a) a transverse cross-section image where all components have been isolated and color coded, and (b) the same cross-section showing how the petal angular positions are determined with respect to the Lorentz force direction.

strand centers were averaged and compared to the center of the conductor itself.

2.2. Individual strand extraction and study

2.2.1. Introduction. Another set of conductor segments (~150 mm long) from the HFZ and from the LFZ were cut using EDM but this time the jacket was removed using an end mill. The released sub-cables were then submerged in a 15% HCl solution for two hours to remove the chromium plating so as to release any sintering that might have occurred during CICC heat treatment. The petals were then separated, the stainless steel wrap removed and the strands color coded with enamel paint according to position. The unraveling of the strands was done with extreme care in order to minimize any additional strain (a video was made of this crucial step). Strand segments about 12 mm long were then cut using wire cutters and these segments were polished in longitudinal orientation. The goal was to extract pieces from the most representative regions of the conductor, so it was decided to pick strands from the HP side, the LP side and four different petal positions as shown in figure 7. In the modeling studies of Bajas *et al* [20] it was predicted that the strands that curved the most during cabling are those that would be most prone to filament fracture, this was also confirmed in [23]. Therefore all extracted strands were classified as ‘bent’ or ‘straight’

depending on the degree of curvature (see strand curvature section). A total of eighty strands were extracted from each conductor, forty from the HFZ and forty from the LFZ. All strands were imaged using the LSCM at 200x magnification which was enough to be able to see filament fractures.

There are two main pieces of information that were obtained from the extracted strands, their crack count and their curvature.

2.2.2. Crack count and analysis. Every LSCM image was carefully inspected for filament fractures and a small digital marker was placed on each crack for subsequent automatic counting. The strands showing filament fractures were then imaged again with backscattered electrons (BSE) in a field emission scanning electron microscope (FESEM) in order to image the cracks at higher magnification and check for additional signs of any post heat treatment strain, in particular cold worked copper grains. Figure 8 shows an example of a strand that developed multiple filament fractures, which also possesses local Cu regions that are significantly cold worked and elsewhere quite strain free. This will be discussed further in the next section.

2.2.3. Strand curvature. In all ITER cables the principal strand curvature is produced by the multiple cabling and twisting stages that are designed to transpose all of the strands to reduce ac losses and to guarantee a uniform current distribution. The curvature mostly depends on the cable twist parameters as well as final compaction of the cable. In addition, some permanent strand curvature may be introduced by the Lorentz force loading as shown qualitatively by the autopsy of the CSJA1 cable [17]. In our earlier autopsy of a SULTAN-tested TF cable [23], we found that almost all filament cracking occurred in curved sections of the strands. Therefore in order to find the probability of having a ‘bent’ strand segment inside the CICC, a separate and much larger set of strand segments around 12 mm long were extracted. To do this, we epoxy impregnated a small length (~10 cm) from one of the six petals for each CICC. Once cured, cuts were done to obtain three 12 mm long pieces of this epoxy impregnated petal. The epoxy was dissolved to release ~450 small strand segments from each sample and these were then submerged in 50% nitric acid in order to completely dissolve the copper strands as we only wanted to measure the curvature of the superconducting strands. Dissolving the copper strands of the CSIO1-2 sample was a crucial step since the pure copper strands are much easier to bend than the Cu/superconductor composite strands [22] and therefore it was expected that the superconducting strands would have less average curvature than the soft copper strands. High resolution flatbed scanner images were then taken of these Cu-stripped strand segments and these images used to measure the end to end separation, d , and the length, l , of each strand as seen in figure 9 for a small number of strands. The ratio d/l defines the strand curvature, c , which in a

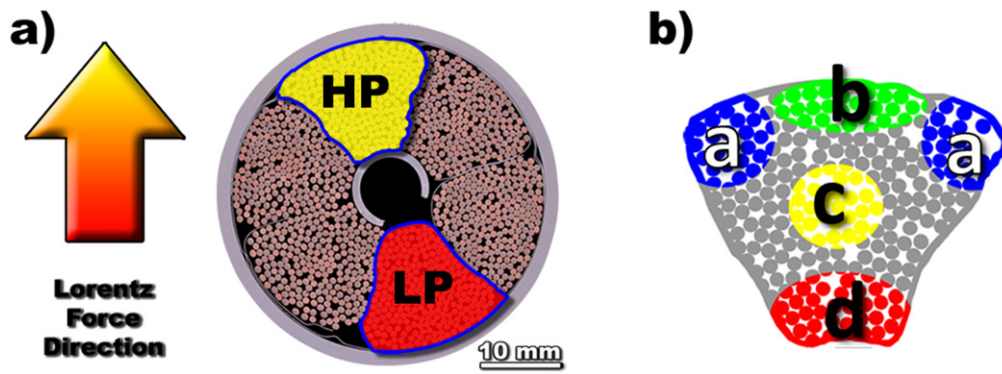


Figure 7. Cable (a) and petal (b) cross-section overviews showing designated regions of interest for the strand extraction study.

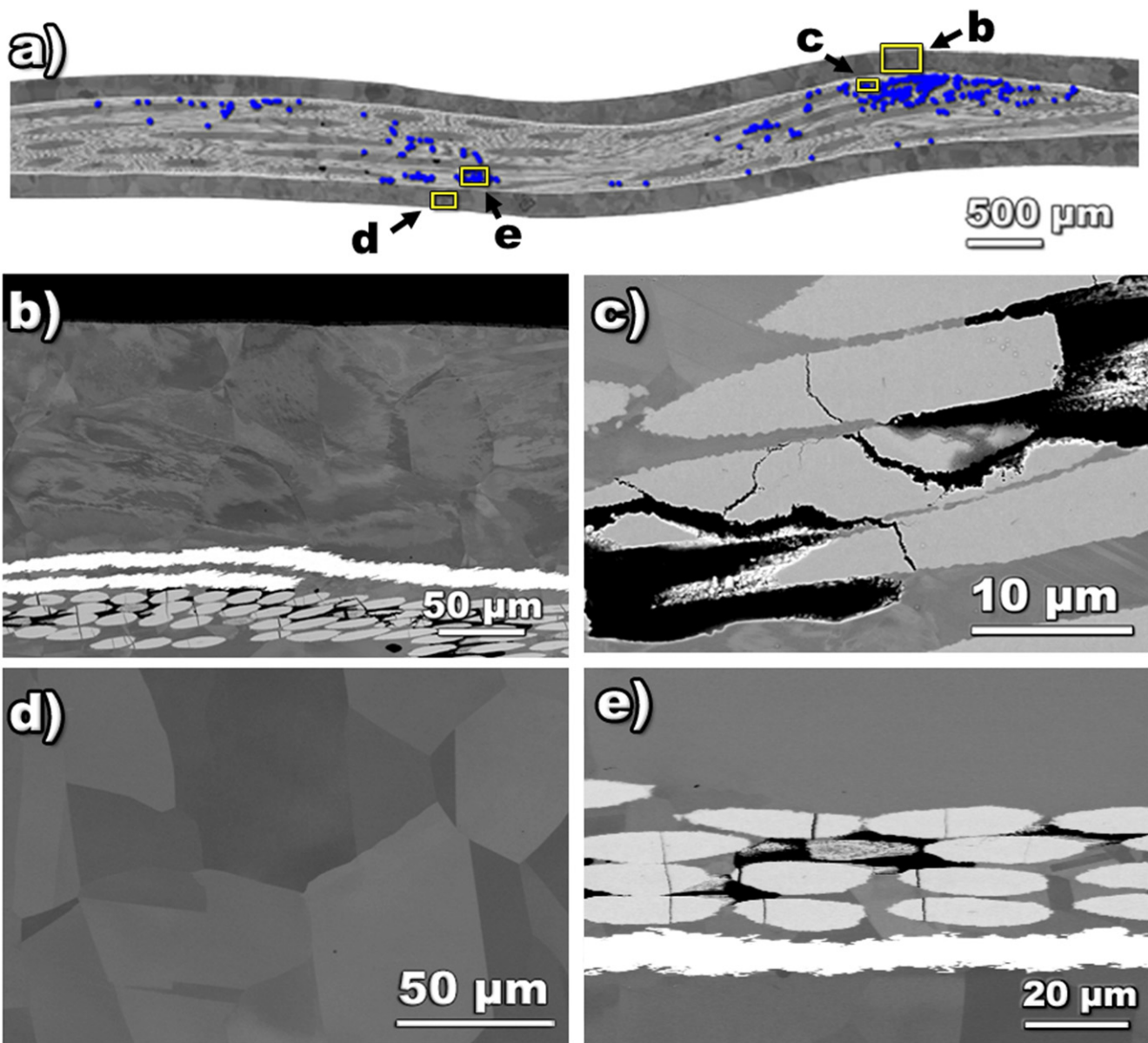


Figure 8. (a) This FESEM–BSE image of a longitudinal cross-section of an extracted strand (CSIO1-1, ‘HP’ side) shows two heavily damaged regions with different filament fracture morphologies (the locations of cracks are shown with digitally applied blue marks). Details in this image show (b) cold worked copper at a contact point with a neighboring strand or jacket, (c) cracks induced by contact stresses, (d) strain free copper grains, and (e) cracks induced by tensile stresses.

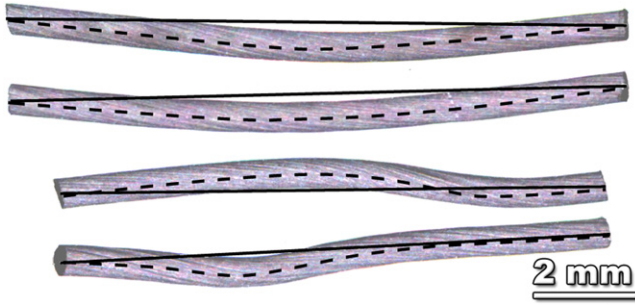


Figure 9. Flatbed scanner images of strands with their stabilization copper etched away used to measure the end-to-end separation, d , (solid line) and the length of the strands, l , (dashed line).

straighter strand approaches 1

$$c = d/l. \quad (1)$$

3. Results

3.1. Transverse cross-section analysis of the void fractions and strand locations

We measured overall void fractions of $33.5 \pm 0.35\%$ and $34.0 \pm 0.30\%$ for the CSIO1-1 and CSIO1-2 CICC, values very close to the calculated values of 33.4% in [1]. We found no difference in these *overall* void fractions between the LFZ and HFZ. The individual petal void fractions for all cross-sections are plotted in figure 10. They show a significant void fraction expansion on the LP side of the HFZ, indicating a migration of the strands from the LP side towards the HP side. This strand migration reduces the strand-to-strand support on the LP side, which is known to be detrimental to cable performance [20, 30].

The deviation of the center of mass of the strands from the center of the cable is shown in figure 11(a) for all cross-sections and their average deviations are shown in figure 11(b). In the LFZ the average positions of the strands are much smaller, slightly off-center ($<100 \mu\text{m}$ overall) and occur in random directions. In the HFZ, however, the strand offsets lie within $\pm 30^\circ$ from the direction of the Lorentz force (0°). Clearly most of the ($\sim 320\text{--}400 \mu\text{m}$) offset in the HFZ is due to strand migration in the direction of the Lorentz force. And although we cannot exclude a small $\sim 100 \mu\text{m}$ random component (as found by the LFZ measurements), the lower offset values in the CSIO1-1 point to a higher stiffness than the CSIO1-2.

Another way of appreciating the influence of pure copper strands is by looking at the strand contact points. Figure 12 shows transverse cross-sections of the two conductors with the strands shaded according to their nearest neighbor number [23]. The number ranges from 0 for strands with no supporting neighbors (i.e. a strand which is not in contact with any other strand) to 5 for strands with five contact points. The segregation of the light and dark regions is much more discernable for the less stiff, Cu-strand-containing CSIO1-2 than

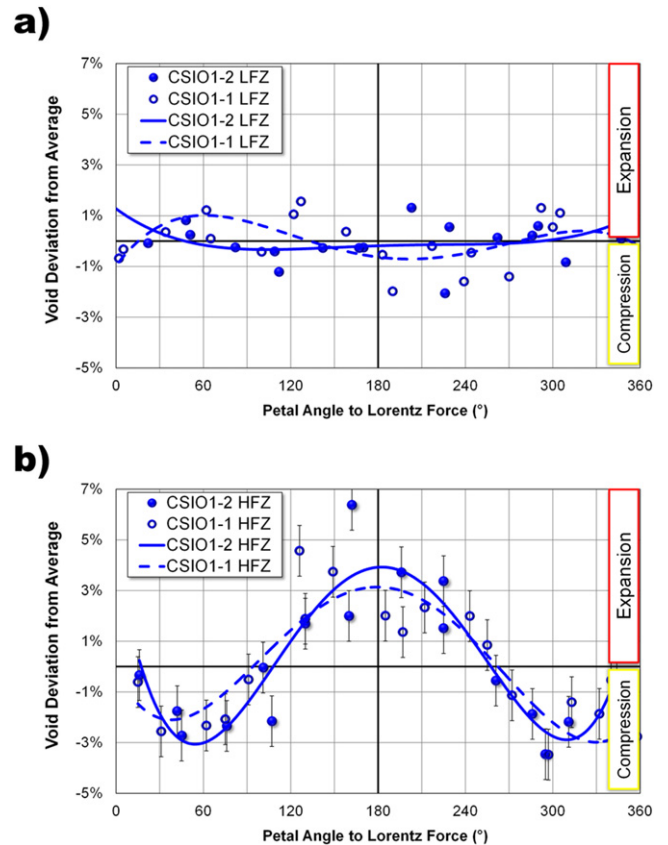


Figure 10. Petal void fraction deviation as a function of petal position with respect to the Lorentz force. Petals in the vicinity of 180° are on the LP side. The trend lines are fourth order polynomial fits to guide the eye.

for all-superconducting CSIO1-1—indicating more plasticity coming from the copper strands.

3.2. Strand curvature

The bell curves that correspond to the statistical values (i.e. average and standard deviation) obtained from the curvature measurements $c = d/l$ (1) of each sample are shown in figure 13 where it can be seen that the probability of finding a curved strand ($c < 0.95$) is much higher for the all superconducting CSIO1-1 CICC (0.21) than for the mixed strand CSIO1-2 CICC (0.08).

3.3. Extracted strand analysis and search for cracks in longitudinal cross-sections

3.3.1. Introduction. Below we present the results obtained via strand extraction but first we must establish the different fracture types observed as they are a significant part of the discussion below.

3.3.2. Filament fracture classification. We found no evidence of filament fracture or cold work in any strands extracted from the LFZ of the CICC samples. We take this to indicate that the axial compression produced during cool-down (the main

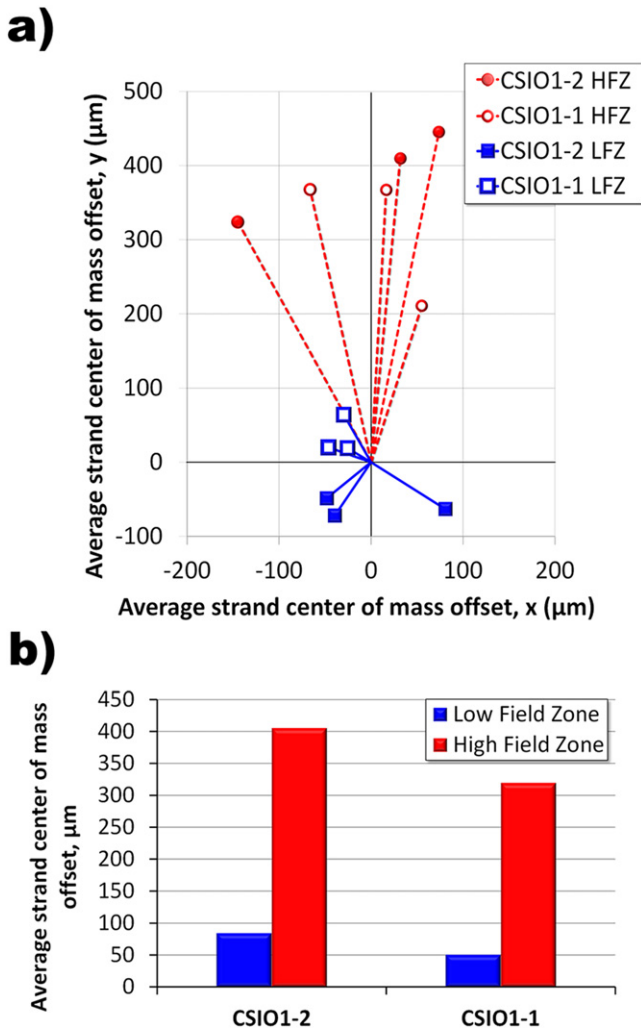


Figure 11. Average strand geometric center offset from the center of the CICC sections (a) and their average movement (b). The offset direction of the HFZ is within $\pm 30^\circ$ of the Lorentz force direction while in the LFZ the movement is smaller and more random.

source of strain in the LFZ) is not high enough to produce filament fractures. It also shows that our CICC deconstruction techniques do not produce false positive cracking.

There was, however, a small population of strands in the HFZ of both CICC sections that developed filament fractures especially in strands with curvature ratios smaller than 0.95. To our surprise, some fractures were not perfectly orthogonal to the filament axis, which is not expected from a brittle material fracturing under tension. We have observed this type of unusual crack in strands tested in TARSIS under conditions designed to simulate pinching or high contact stresses [22]. These high-angle cracks are readily distinguishable from low angle cracks produced in a pure bending configuration where the tensile stresses produced by bending initiate cracks. Figure 14 shows examples of cracks at high angles produced by pinching and low angle cracks produced by bending during TARSIS testing. For this paper, based on the TARSIS results, we classify the cracks with angles of less than 15° as Type A strand bending cracks, while those cracks

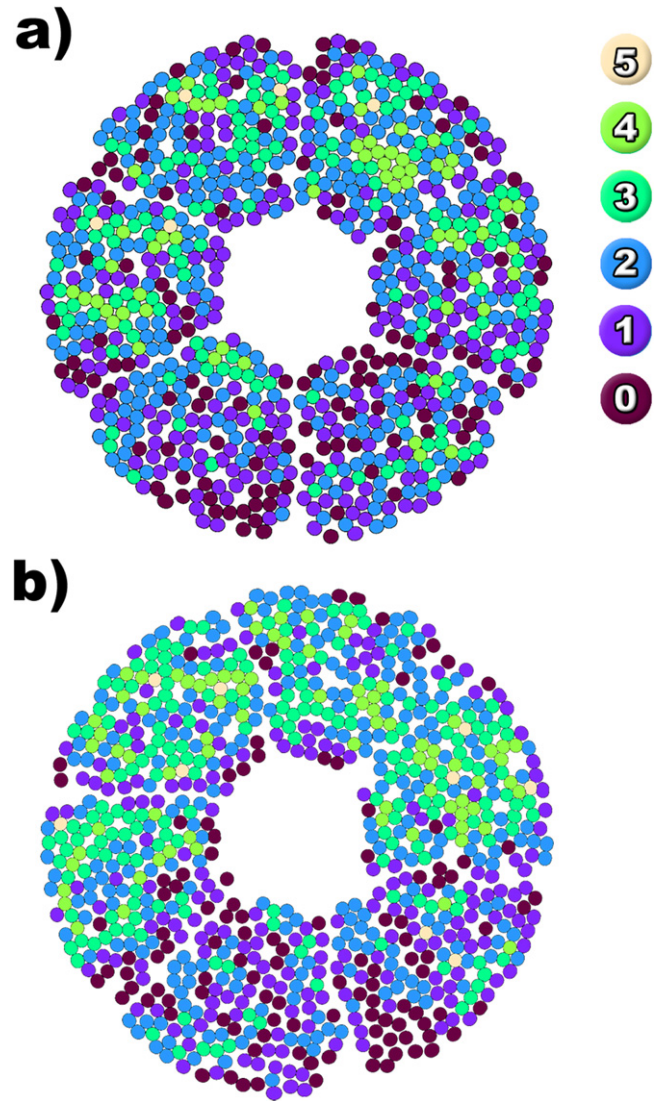


Figure 12. Transverse cross-sections of the HFZs of (a) CSIO1-1 without copper strands and (b) CSIO1-2 with copper strands. The strands are shaded according to the adjacent strand count (i.e. number of nearest-neighbor strands), which ranges from 0 to 5.

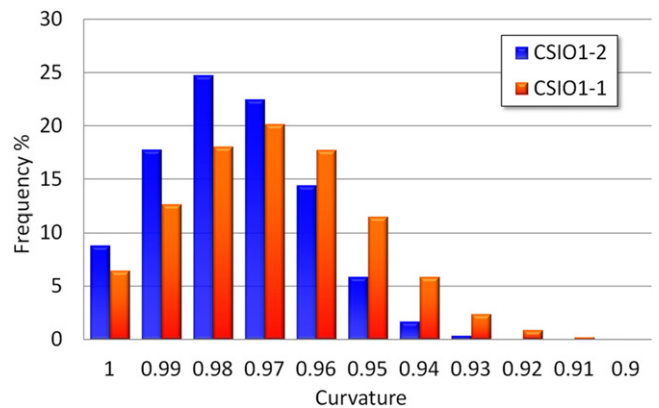


Figure 13. Distribution of the curvature of extracted strand pieces according to their curvature parameter, c .

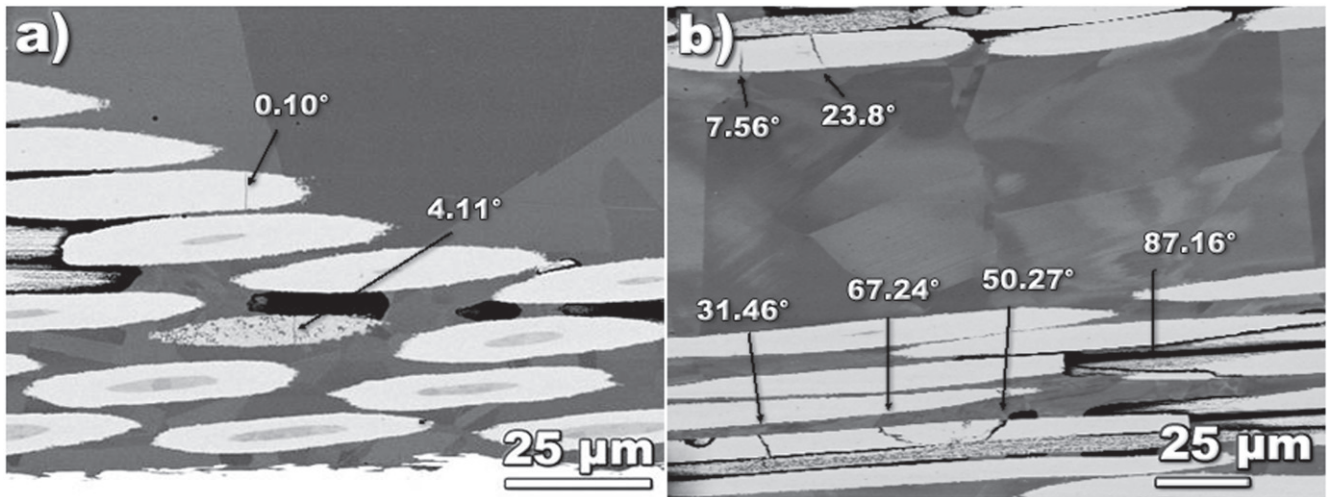


Figure 14. Two different types of filament fractures are developed in internal tin strands during TARSIS testing: (a) tensile fractures characterized by small angles to the plane orthogonal to the filament axis and (b) contact stress fractures characterized by a higher angle that are usually seen in the vicinity of cold worked copper grains.

Table 2. Filament fracture count on each strand extracted from the CSIO1-2 (Cu and superconducting strands) sample.

	HP bent	HP straight	LP bent	LP straight
a	0	0	0	3
a	0	0	0	37
b	0	0	79	0
b	0	0	152	20
a	0	0	460	9
a	0	0	—	0
c	0	0	0	0
c	0	0	—	0
d	0	0	0	0
d	0	0	0	0
Ave.	0	0	86.4	6.9

Table 3. Filament fracture count on each strand extracted from the CSIO1-1 (superconducting strands only) CICC.

	HP bent	HP straight	LP bent	LP straight
a	—	16	8	4
a	22	3	3	2
b	68	4	28	0
b	4	15	0	0
a	0	0	0	0
a	334	0	165	7
c	—	5	—	2
c	—	0	5	26
d	—	25	7	0
d	6	0	0	3
Ave.	72.3	6.8	24	4.4

with angles higher than 15° are defined as Type B strand pinching or contact cracks. The angle is measured between the local wire axis and the direction of the crack.

3.3.3. Crack count and analysis. The crack counts for each piece of strand extracted from the HFZ are shown in tables 2 and 3. It became apparent very quickly that the population of strands with filament fractures is not directly related to the performance of the cables—since more of these were found in the better-performing CSIO1-1. In tables 2 and 3 strands labeled as ‘bent’ have a stronger curvature with ratios lower than 0.95, while straight strands have a curvature ratio higher than 0.98 (strand pieces with intermediate values of curvature were not used). The strands are arranged according to their respective petal and cable positions denoted in figure 7. Empty cells in tables 2 and 3 are strand pieces where we failed to obtain an acceptable cross-section.

An important result on strands extracted from CSIO1-2, that contains both Cu and superconducting strands, is that we

found no filament fractures on the HP side but we did find some strands with a significant crack density on the LP side. The most damaged strand from CSIO1-2 is shown in figure 15 and the crack locations are highlighted with blue dots. This strand had more than 95% Type A cracks and since the fractures were located on a single side of the strand we can assume that this was on the tensile side of the bend, as previously observed in TF cable [23]. The overall population of filament fractures in this CSIO1-2 sample is 93% Type A and 7% Type B which are ratios comparable to our observations on samples tested in bending with TARSIS [22].

In contrast to the CSIO1-2, the all superconducting CSIO1-1 has several strands with a wide variety of crack densities (table 3). The most damaged strand extracted from the HP side is shown in figure 8 where only 20% of the cracks were Type A. In fact all the strands showing fractures in the HP side were Type B crack dominant. Due to their evident frequency in the CSIO1-1, it appears that Type B cracks do not have a strong impact on the performance of the cable.

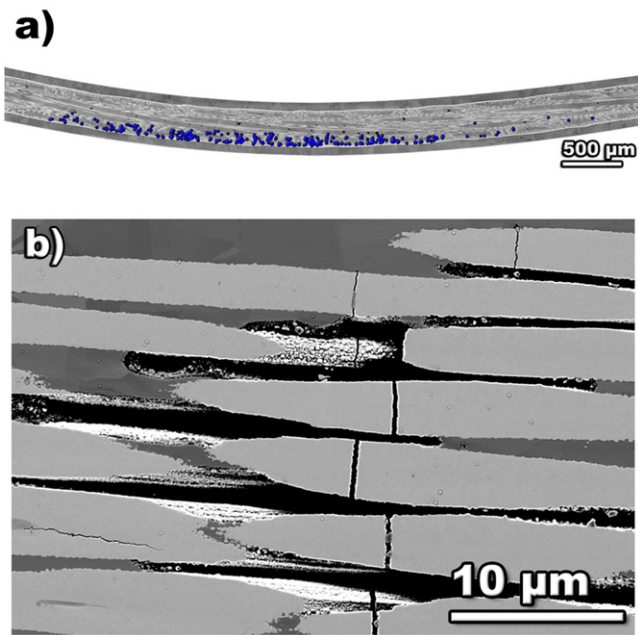


Figure 15. (a) Longitudinal cross-section of a strand extracted from the LP side of the CSIO1-2 HFZ CICC with crack locations highlighted using blue dots. (b) A closer view that shows a predominance of Type A cracks.

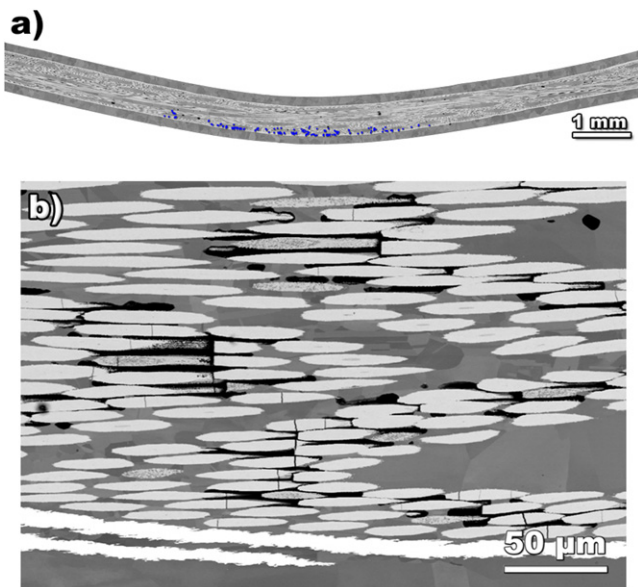


Figure 16. (a) Longitudinal cross-section of a strand extracted from the LP side of the CSIO1-1 CICC with the crack locations highlighted using blue dots on the outer curvature where tensile stresses are expected. (b) A magnified view shows a predominance of Type A cracks.

Type A cracks on the other hand have a similar pattern in the LP side of both conductors, with the CSIO1-1 having an overall lower average number (see LP side in tables 2 and 3). A strand from the LP side of the CSIO1-1 sample is shown in figure 16. It presents a very similar fracture pattern to the CSIO1-2 strand from figure 15, consistent with bending-induced cracks.

In summary, the overall crack population in the HP side of this CSIO1-1 sample is 36% Type A bending cracks and 64% Type B pinch cracks, while on the LP side, we found 80% Type A and 20% Type B—yielding a much lower overall number of Type A cracks in the CSIO1-1 sample.

4. Discussion

There is clear evidence that the Lorentz force induced by the SULTAN magnetic field produces transverse movement of the strands towards the HP side in these ITER prototype cables (figure 11) and that the overall strand migration is lower for the superconductor-only cable (CSIO1-1). This strand migration inherently leaves a greater void fraction on the LP side (figure 10), which is a condition known to allow higher strand bending in a CICC under magnet operation [20, 30]. High *tensile stress states* due to bending are therefore an important source of degradation in a CICC, and in extreme cases Type A cracks are manifested. Conversely, high *compressive stress states* due to pinching seem to have a lower impact on the degradation of the CICC since Type B cracks were quite common in the all-superconducting and better performing CSIO1-1 cable. It should be noted that Type B cracks were rarely located any further than $\sim 400 \mu\text{m}$ from the pinching point. This suggests that the high *compressive stress state* produced by strand contact in the HP side of the conductor may not have a significant impact on the T_{cs} —or simplistically Type A cracks are much more detrimental than Type B cracks, or better yet, the stress state under which the Nb_3Sn finds itself around a Type A crack is more detrimental.

The replacement of pure Cu strands with superconducting (Cu/Superconductor) composite strands increases the stiffness of the six CSIO1-1 sub-cables and it reduces the Lorentz force applied to each individual strand. It is thus reasonable to predict a lower strand movement (figure 11) and a smaller void fraction expansion on the LP side (figure 10). Additionally, looking at the strand cross-sections of figure 2(a), the outermost filaments of the strand in the CSIO1-1 cable are closer to the neutral axis ($251 \mu\text{m}$ from the center of the strand) than in the CSIO1-2 case ($278 \mu\text{m}$ from the neutral axis) lowering further the potential of high tensile strains in bending for the CSIO1-1. A strong indication that the peak bending strains were indeed lower in the CSIO1-1 conductor is the fact that the average crack count found (per strand piece) on the LP side was 72% lower than in the CSIO1-2 (24.0 cracks versus 86.4, see tables 3 and 2). All of these observations may explain the lower T_{cs} degradation of the CSIO1-1 CICC but it must be noted that this conductor design, stiffer though we expect it to be, did not eliminate the initial degradation.

The importance of conductor and strand stiffness becomes even more apparent when the *bronze* baseline CICC CS prototype is analyzed. This bronze design (CSJA2-2) was tested in SULTAN prior to CSIO1-1 and CSIO1-2 testing. It underwent 14 000 cycles and two warm-up/cool-down cycles [17]. It also had the same twist pitch and cable design as the

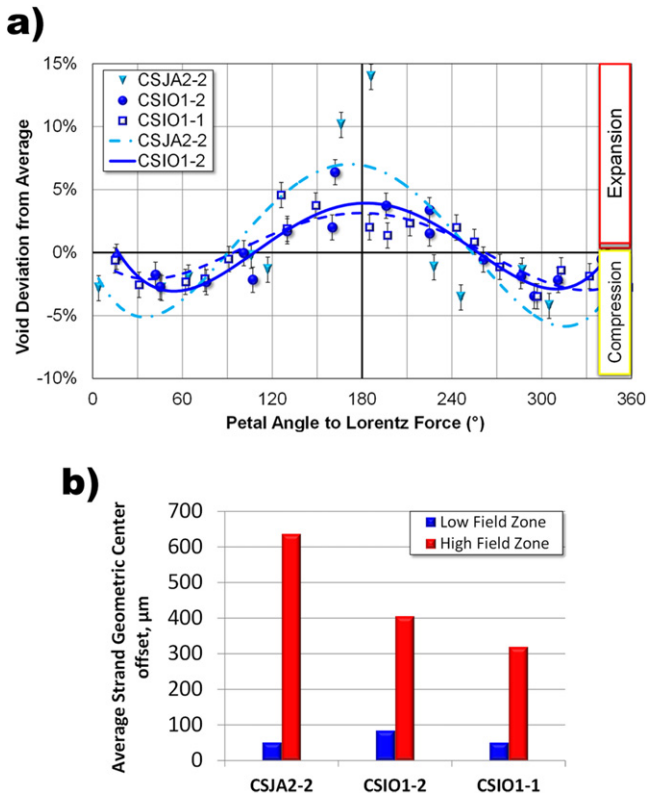


Figure 17. (a) Petal void fraction deviation as a function of petal position with respect to the Lorentz force. (b) Average offset of strand geometric center.

CSIO1-2, differing only in substituting the internal tin strands (seen here) for 3^d generation bronze process strands [18, 19], which are inherently less stiff than internal tin strands [22]. The autopsy of CSJA2-2 was also performed by our group and we found that this CSJA2-2 had a (1) higher crack population [30], (2) an enhanced void fraction redistribution (figures 17(a)) and (3) an average strand movement 60% higher than that of CSIO1-2 (figure 17(b)). In this case the SULTAN tests resulted in a sharper T_{cs} drop than the CSIO1-2 and it showed no signs of T_{cs} stabilization even after 10 000 cycles [9, 17] indicating that stiffness is a desired property of CICC (this will be discussed further in a second article).

5. Conclusion

The CSIO1-1 and CSIO1-2 samples were tested as part of the ITER prototype conductor development program in order to understand the role of copper strands in the first triplet cabling stage of the CICC. The better-performing CSIO1- cable (with no Cu strands and an overall superconducting area increase of about 20%) led to less strand movement and had a lower number of Type A cracks (associated with bending). However, this conductor often exhibited compressive-like filament fractures which we denominated Type B cracks. The location of these Type B cracks is limited to $\sim 400 \mu\text{m}$ from the strand cross-over (pinching) point and their presence does not seem to have a significant impact on the T_{cs} degradation.

The use of copper strands in the CSIO1-2 sample suppressed the formation these Type B filament cracking on the HP side of the conductor, probably due to the soft Cu absorbing some of the compression that is associated with the Type B cracks. High contact stress points deduced from local cold work at contact points were not found in the mixed strand CSIO1-2 CICC while they were common on the HP side of the all-superconducting CSIO1-1 CICC, suggesting that the copper strands do reduce the local contact stresses (despite the higher Lorentz force of the superconducting strands). However, if there is any benefit to this crack prevention mechanism it is not reflected in the T_{cs} evolution of the conductor. On the other hand the presence of Type A cracks (found only on the LP side of the conductor) seems to agree more with the performance of the conductors.

Although changing the components of the triplet in these otherwise identical cables significantly changed the location and type of Nb₃Sn filament cracking found after cyclic SULTAN tests, the strand movement during testing was still sufficient to produce an appreciable rate of degradation. In the next part of this study we will compare these conductors with two subsequent prototypes where strand movement was sufficiently suppressed to eliminate degradation.

DISCLAIMER: The views and opinions expressed here do not necessarily reflect those of the ITER organization

Acknowledgments

The CICC were provided by courtesy of Pierluigi Bruzzone (CFRP Villigen, CH) with agreement from ITER-IO and USIPO. This work was supported by the ITER-IO under purchase order ITER/CT/11/4300000511, US-ITER under contract 6400011187, and the US Department of Energy Office of Fusion Energy Sciences under award DE-FG02-06ER54881. The National High Magnetic Field Laboratory where the experiments were performed is supported by the National Science Foundation Cooperative Agreement DMR-1157490 and by the State of Florida.

References

- [1] Devred A, Backbier I, Bessette D, Bevilard G, Gardner M, Jong C, Lillaz F, Mitchell N, Romano G and Vostner A 2014 Challenges and status of ITER conductor production *Supercond. Sci. Technol.* **27** 044001
- [2] Mitchell N, Devred A, Libeyre P, Lim B and Savary F 2012 The ITER magnets: design and construction status *IEEE Trans. Appl. Supercond.* **22** 4200809
- [3] Mitchell N, Bessette D, Gallix R, Jong C, Knaster J, Libeyre P, Sborchia C and Simon F 2008 The ITER magnet system *IEEE Trans. Appl. Supercond.* **18** 435–40
- [4] Marken K 2012 1—Fundamental issues in high temperature superconductor (HTS) materials science and engineering *High Temperature Superconductors (HTS) for Energy Applications* ed Z Melhem (Cambridge: Woodhead) pp 1–31
- [5] Cooley L D, Ghosh A K and Scanlan R M 2005 Costs of high-field superconducting strands for particle accelerator magnets *Supercond. Sci. Technol.* **18** R51

- [6] Ekin J W 1981 Mechanical properties and strain effects in superconductors *Superconductor Materials Science: Metallurgy, Fabrication, and Applications* ed S Foner and B B Schwartz (Berlin: Springer) pp 455–510
- [7] Martovetsky N *et al* 2002 Test of the ITER central solenoid model coil and CS insert *IEEE Trans. Appl. Supercond.* **12** 600–5
- [8] Mitchell N 2007 Assessment of conductor degradation in the ITER CS insert coil and implications for the ITER conductors *Supercond. Sci. Technol.* **20** 25
- [9] Devred A, Backbier I, Bessette D, Bevilard G, Gardner M, Jewell M, Mitchell N, Pong I and Vostner A 2012 Status of ITER conductor development and production *IEEE Trans. Appl. Supercond.* **22** 4804909
- [10] Bruzzone P, Stepanov B and Wesche R 2009 Qualification tests for ITER TF conductors in SULTAN *Fusion Eng. Des.* **84** 205–9
- [11] Bruzzone P, Wesche R, Stepanov B, Cau F, Bagnasco M, Calvi M, Herzog R and Vogel M 2009 Qualification tests and facilities for the ITER superconductors *Nucl. Fusion* **49** 065034
- [12] Bruzzone P, Anghel A, Fuchs A, Pasztor G, Stepanov B, Vogel M and Vecsey G 2002 Upgrade of operating range for SULTAN test facility *IEEE Trans. Appl. Supercond.* **12** 520–3
- [13] Bruzzone P *et al* 2008 Results of a new generation of ITER TF conductor samples in SULTAN *IEEE Trans. Appl. Supercond.* **18** 459–62
- [14] Breschi M *et al* 2012 Results of the TF conductor performance qualification samples for the ITER project *Supercond. Sci. Technol.* **25** 095004
- [15] Martovetsky N N, Hatfield D R, Miller J R, Bruzzone P, Stepanov B and Seber B 2010 Qualification of the US-made conductors for ITER toroidal field (TF) magnet system *IEEE Trans. Appl. Supercond.* **20** 466–9
- [16] Tronza V I, Lelekhov S A, Stepanov B, Bruzzone P, Kaverin D S, Shutov K A and Vysotsky V S 2014 Test results of RF ITER TF conductors in the SULTAN test facility *IEEE Trans. Appl. Supercond.* **24** 1–5
- [17] Hemmi T *et al* 2012 Test results and investigation of T_{cs} degradation in Japanese ITER CS conductor samples *IEEE Trans. Appl. Supercond.* **22** 4803305
- [18] Miyatake T, Murakami Y, Kurahashi H, Hayashi S, Zaitso K, Seeber B, Mondonico G and Nabara Y 2012 Influence of wire parameters on critical current versus strain characteristics of bronze processed superconducting wires *IEEE Trans. Appl. Supercond.* **22** 4805005
- [19] Devred A *et al* 2013 Status of conductor qualification for the ITER central solenoid *IEEE Trans. Appl. Supercond.* **23** 6001208
- [20] Bajas H, Durville D, Ciazynski D and Devred A 2010 Numerical simulation of the mechanical behavior of ITER cable-in-conduit conductors *IEEE Trans. Appl. Supercond.* **20** 1467–70
- [21] Nijhuis A and Ilyin Y 2006 Transverse load optimization in Nb₃Sn CICC design; influence of cabling, void fraction and strand stiffness *Supercond. Sci. Technol.* **19** 945
- [22] Nijhuis A *et al* 2013 The effect of axial and transverse loading on the transport properties of ITER Nb₃Sn strands *Supercond. Sci. Technol.* **26** 084004
- [23] Sanabria C, Lee P J, Starch W, Pong I, Vostner A, Jewell M C, Devred A and Larbalestier D C 2012 Evidence that filament fracture occurs in an ITER toroidal field conductor after cyclic Lorentz force loading in SULTAN *Supercond. Sci. Technol.* **25** 075007
- [24] Calzolaio C, Bruzzone P and Uglietti D 2012 Measurement of T_c distribution in Nb₃Sn CICC *Supercond. Sci. Technol.* **25** 054007
- [25] Pong I 2012 *Private communication*
- [26] March S A, Bruzzone P, Stepanov B, Bessette D, Boutboul T, Devred A, Mitchell N, Readman P and Vostner A 2013 Results of the TFEU6 sample tested in SULTAN *IEEE Trans. Appl. Supercond.* **23** 4200204
- [27] Hemmi T, Harjo S, Nunoya Y, Kajitani H, Koizumi N, Aizawa K, Machiya S and Osamura K 2013 Neutron diffraction measurement of internal strain in the first Japanese ITER CS conductor sample *Supercond. Sci. Technol.* **26** 084002
- [28] Nabara Y *et al* 2012 Examination of Japanese mass-produced conductors for ITER toroidal field coils *IEEE Trans. Appl. Supercond.* **22** 4804804
- [29] SULTAN-Team C 2002 User specifications for conductor samples to be tested in the SULTAN facility *EPFL Library* (<http://infoscience.epfl.ch/record/121266>)
- [30] Mitchell N, Devred A, Larbalestier D C, Lee P J, Sanabria C and Nijhuis A 2013 Reversible and irreversible mechanical effects in real cable-in-conduit conductors *Supercond. Sci. Technol.* **26** 114004
- [31] Schindelin J *et al* 2012 Fiji: an open-source platform for biological-image analysis *Nat. Methods* **9** 676–82
- [32] Schneider C A, Rasband W S and Eliceiri K W 2012 NIH image to imagej: 25 years of image analysis *Nat. Methods* **9** 671–5
- [33] Bruzzone P 2004 The index n of the voltage–current curve, in the characterization and specification of technical superconductors *Physica C* **401** 7–14